

# Scalable Path Level Thermal History Simulation of PBF process validated by Melt Pool Images

Xin Liu<sup>a</sup>, Xingchen Liu<sup>a,\*</sup>, Goldy Kumar<sup>a</sup>, Paul Witherell<sup>b</sup>

<sup>a</sup>*Intact Solutions, Inc.*

<sup>b</sup>*National Institute of Standards and Technology*

## Abstract

The thermal history of the powder bed fusion (PBF) process is critical due to its significant influences on the material properties, residual stress, and part warping or distortion. These quantities heavily affect the quality and performance of parts. The contact-aware path-level (CAPL) discretization approach [1, 2, 3] was recently proposed to support scalable thermal simulation at the path level of AM processes driven by a moving heat source. Compared to other thermal simulation approaches, CAPL tailors discretization to the manufacturing toolpath and adopts locality for linear time complexity in part-scale thermal history simulations. This approach essentially uses scalable simulations to simulate the fabrication process of a part through the aggregation of melt pools, scan paths, and layers.

In this paper we outline the development of a scalable PBF thermal history simulation built on CAPL and based on melt pool physics and dynamics. The new approach inherits linear scalability from CAPL and has three novel ingredients. Firstly, to simulate the laser scanning on a solid surface, we discretize the entire simulation domain instead of only the manufacturing toolpath by appending fictitious paths to the manufacturing toolpath. Secondly, to simulate the scanning on overlapping toolpaths, the path-scale simulations are initialized by a Voronoi diagram for line segments discretized from the manufacturing toolpath. Lastly, we propose a modified conduction model that considers the high thermal gradient around the melt pool. We validate the simulation against melt pool images captured with the co-axial melt pool monitoring (MPM) system on the NIST Additive Manufacturing Metrology Testbed (AMMT). Excellent agreements in the length and width of melt pools are found between simulations and experiments conducted on a custom-controlled laser powder bed fusion (LPBF) testbed on a nickel-alloy (IN625) solid surface. To the authors' best knowledge, this paper is the first to validate a full path-scale thermal history with experimentally acquired melt pool images. Comparing the simulation results and the experimental data, we discuss the influence of laser power on the melt pool length on the path-scale level. We also identify the possible ways to further improve the accuracy of the CAPL simulation without sacrificing efficiency.

**Keywords:** Additive manufacturing; Powder bed fusion; Thermal history simulation; Laser melt pool

## 1. Introduction

Laser powder bed fusion (LPBF) additive manufacturing (AM) uses lasers as moving heat sources to melt and solidify thin layers of metal powder along a predefined tool path layer by layer [4, 5, 6]. Many complex multi-physics and multi-phase phenomena are involved in the different stages of the LPBF process, including the initial melting of metal powders, the fluid dynamics and heat transfer of the molten metal, and the stresses and microscopic grain structure resulting from the solidification of liquid metals. These phenomena have important influences on the quality and performance of the manufactured part. As many of them are related to the thermal history of the part, an accurate and efficient thermal history simulation becomes critical to the understanding and improvement of LPBF

processes. For example, thermal history influences the microstructure [7] and the material properties [8, 9]. The thermal history also influences the part's geometric accuracy through the residual stress, which is caused by uneven thermal expansion and shrinkage [10], which is closely related to the thermal history of LPBF parts.

The thermal history of a specific part is the result of its manufacturing process plan. The process plan includes processing parameters (e.g., the environmental and pre-heating temperature of the platform) and path-dependent scanning information including the power and speed of the laser. For a given geometric model, the build direction is determined first. Based on the process specifications such as the powder layer thickness, the geometric model is then sliced into layers normal to the building direction. Finally, the layers from slicing are filled with scanning paths, which direct the laser to scan the path segments with the given laser power. The scanning paths have a critical influence on thermal history. For example, a given location might be melted once or remelted multiple times if different scanning paths are adopted. For a given geometric model, different combinations of possible building

\*Corresponding author

Email addresses: xin@intact-solutions.com (Xin Liu), xliu@intact-solutions.com (Xingchen Liu), gkumar@intact-solutions.com (Goldy Kumar), paul.witherell@nist.gov (Paul Witherell)

directions and scanning path results in an enormous degree of freedom on the path-scale level for process plan designing. The complexity of scanning patterns and the utilization of fast-moving and high-energy lasers in LPBF processes lead to complex heating/cooling and phase transitions, which complicates the thermal history across the entire part. Path-scale simulation approaches are critical to predicting the thermal history and exploring different process plans.

We develop a scalable PBF thermal simulation approach based on CAPL. CAPL tailors discretization to the manufacturing toolpath and adopts locality for linear time complexity in part-scale thermal history simulations. The new approach (will be referred as PBF-CAPL) inherits linear scalability from CAPL and has three novel ingredients. Firstly, to simulate the laser scanning on a solid surface, we discretize the entire simulation domain instead of only the manufacturing toolpath by appending the fictitious paths to the manufacturing toolpath. Secondly, to simulate the scanning on the overlapping toolpath, the element widths are initialized by a Voronoi diagram of the manufacturing toolpath. Lastly, we propose a modified conduction model that considers the high thermal gradient around the melt pool. We validate the new approach against melt pool images captured with the co-axial melt pool monitoring (MPM) system on the Manufacturing Metrology Testbed (AMMT) developed at the National Institute of Standards and Technology (NIST) [11, 12]. Excellent agreements in the length and width of melt pools are found between simulations and experiments conducted on a custom-controlled laser powder bed fusion (LPBF) testbed on a nickel-alloy (IN625) solid surface.

The rest of the paper is organized as follows. We review the related work in the next section. For the sake of completeness, we provide an overview of the original CAPL approach in Section 2.3. In Section 3, we identify and implement the needed improvements to account for the limitations of the original CAPL and specifics of the validation dataset.

In Section 4, we validate the simulation results against the experimental dataset that includes scan paths with varying laser power, where we find good agreement in the melt pool shapes between simulation results and the experimental dataset. In addition to comparing the melt pool images frame by frame, we also analyze various trends observed in the dataset. These include the influence of laser power on melt pool length, the melt pool length evolution on the same scanning vector, and scan-wise melt pool length evolution.

Based on the observation in Section 4, Section 5 discusses further improvements to CAPL-based thermal history simulation. These include the incorporation of the laser absorptivity model affected by surface roughness and keyholes and utilizing machine learning to determine melt pool shapes.

## 2. Related Work

### 2.1. LPBF in-process temperature measurements

Two main types of experimental temperature measurements in the LPBF process are often used for in-process

temperature measurements in LPBF: (a) Thermocouples and devices which can measure temperature at specific locations [13, 14]. (b) “co-axial” approaches [15] or “off-axis” approaches [16] thermal camera imaging and pyrometry devices that can measure heatmap and heating/cooling profiles [17] of the layer or the local region around the melt pool [18]. Such direct temperature measurement of melt pool temperature measurement usually involves the estimation of melt pool radiation, which can be modeled by the Sakuma-Hattori equation [19]. In such measurements, it is required to have the delicate calibration of surface properties such as emissivity, which is difficult to estimate due to fast phase transitions like evaporation or liquidation [20]. In the LPBF process, researchers tried to directly use the raw data. For example, local overheating can be detected by “hot spots” via high-speed video imaging [21, 22]. Measured quantities like melt pool shapes [23] or other process by-products including spatters and plumes are also used in papers [24, 25] to study the thermal history indirectly.

In this paper, we use the melt pool shape as our experimental data for validation. The shape of the melt pool is a direct result of the thermal history. For example, high energy input or high residual heat caused by nearby scanning might lead to a larger melt pool shape. The melt pool length and width reflect the anisotropy of the thermal history. By analyzing the melt pool shape, it is possible to gain insight into the thermal history of the process and make adjustments to optimize the resulting product. For example, the melt pool shape has been used to predict overheating or underheating thermal defects in paper [26].

The melt pool shape data we used is generated by the Additive Manufacturing Metrology Testbed (AMMT). AMMT is a fully custom, open-platform laser powder bed fusion system built by the National Institute of Standards and Technology (NIST) [27, 28]. This platform uses co-axial melt pool monitoring (MPM) camera, which is capable of taking high-speed high-resolution melt pool frames [29]. Much research has been conducted with MPM images. For example, Zhang et al. [30] built a data-driven melt pool prediction model using AMMT data to keep the melt pool size as constant as possible. Ho et al. [31, 32] present a new laser power control algorithm that scales the laser power to reduce the variability of melt pool intensity measured throughout the 3D build based on AMMT melt pool data. These papers demonstrated that the melt pool frames can provide highly valuable information even without calibrated temperature distribution.

### 2.2. Numerical simulation of LPBF thermal history

Alternatively, computer simulation can be used to predict LPBF thermal history. Generally speaking, simulation approaches can be categorized into micro-level, path-level, and part-level simulation. The micro-level simulation requires high-fidelity modeling of multiphysics including powder dynamics, fluid dynamics of molten metal, and the interaction between molten metals and metal powders, to list a few [33]. The micro-level simulation, therefore, is computationally expensive and often limited to a short printing path. The finite element method (FEM) is a common approach [34, 35, 36] to simulate the path level LPBF

process. Compared to micro-level simulation, FEM-based approaches simplify the complex multiphysics problem inside the melt pool. However, a naive implementation of FEM is still computationally expensive because it not only requires small time steps to resolve the high cooling rate at more than  $100\text{ }^{\circ}\text{C/s}$  [7], but also maintains a high spatial resolution to capture large size difference between melt pools (100  $\mu\text{m}$ ) and printed part (10-100 mm).

The need for high discretization resolution, small time steps, and the associated high computational costs prohibits the broader adoption of FEM-based approaches in practical engineering applications. For example, only a single-scan path and simple scan strategies are simulated on the path level due to the high computational cost in [37] and [38], respectively. In comparison, a  $2\text{ mm} \times 2\text{ mm}$  3-layer structure may require up to 10 hours to simulate [36]. As a result, many consider path-level simulations too computationally expensive to be practical for engineering applications [39, 40]. Multiscale and agglomeration techniques, such as inherent strain [41] and flash heating [42, 43], have been proposed to bypass the computational complexity in the part-level thermal history simulation. In these methods, the thermal history on the path-scale level is assumed to be uniform so that it can be “lumped” or “agglomerated” on the layers. The loss of path-level information in thermal history, in turn, leads to inaccurate downstream simulations of, warping, residual stress, material properties, and the overall performance of the part [44, 40], to list a few. Graph theory [45] is introduced to make a more efficient simulation of the LPBF process. Adaptive mesh [46] is also introduced to alleviate the computational cost. The effect of scanning strategies in the LPBF process is investigated in papers [47, 48, 49], where post-process measurements such as stresses are used to validate their approaches. In summary, the state-of-the-art thermal history simulation approaches are either too computationally expensive or not accurate enough due to unaccounted assumptions.

### 2.3. Overview of CAPL

A Contact-aware path-level (CAPL) discretization approach was recently developed for simulating the path-level thermal history of a moving heat source [1, 2, 3]. The CAPL approach was proposed to improve the state-of-the-art in two aspects: (1) A discretization base on the manufacturing tool path, and (2) a localized thermal history computation based on the contact graph. CAPL has been shown to outperform adaptive remeshing methods [50] in FEM simulation since the remeshing step is very expensive [3].

The CAPL approach was proposed for thermal simulation of the additive manufacturing process driven by a moving heat source, including fused deposition modeling (FDM) [1] and powder bed fusion (PBF) [2, 3]. CAPL consists of a pre-processing stage and an execution stage with multiple components (see Figure 1). In the pre-processing stage, elements are generated by path-level discretization. Then the contact-graph data structure is initialized. In the execution stage, simulation based on the lumped-capacitance heat transfer model assisted by the contact graph and elements. The active body algorithm is

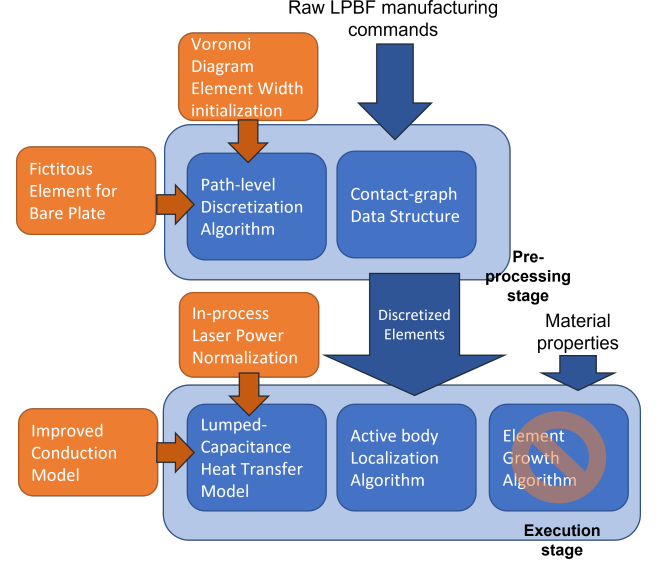


Figure 1: System diagram of contact-aware path-level (CAPL) for laser powder bed fusion (LPBF) process. The components of the original CAPL are in dark blue and our modification and improvements for validation are shown in orange.

used to achieve linear time complexity. The element width and contact graph are updated by the element growth algorithm. For the sake of completeness, we include the following description of components that are relevant to the current work. The interested reader may refer [3] for details.

In the path-level discretization algorithm, the scan path and laser power information are extracted from the input file and discretized in both space and time into some sub-paths. CAPL considers an element to be the material that has been newly melted/sintered by a laser scan along the corresponding sub-path, so each element must correspond to a sub-path with positive laser power. Each element is approximated as a path-aligned box defined by its length  $L$  (equal to the length of the sub-path), width  $W$ , and height  $H$  (equal to the layer height). The cross-sectional shape is a rectangle  $W \times H$  which is perpendicular to the scanning direction. The top surface of the element is approximated by a rectangle  $L \times H$ . The initial width of an element  $W_0$  is predefined. This width will be dynamically grown in the execution stage assisted by the element growth mechanism. The original CAPL approach requires no overlap between different top surfaces of different elements. The connectivity (adjacency information between elements), which is represented by a spatial structure called a contact graph, is initialized with the initialized element positions and sizes. The previous CAPL implementation only supported orthogonal scan paths as it assumed that the elements are aligned.

The element growth mechanism is introduced in the simulation to mimic the powder melting process. Each element is initialized with a small initial width ( $W_0$ ) which is determined by empirical data or high-fidelity simulations. The initial width is always smaller than the final width because thermal expansion will only enlarge the element width. Element width will grow according to its

thermal conditions via an iterative correction procedure in the execution stage. The width growth is triggered when an element's temperature is higher than some predefined threshold which mimics the melting of the element and its thermal width expansion.

The lumped-capacitance heat transfer model is a lumped parameter model which is derived from the energy conservation of laser energy input  $H$ , radiation  $Q$ , convection  $Q_{conv}$ , and conduction  $Q_{cond}$ . The lumped parameter models have been commonly used in many engineering systems [51] to represent the spatially and temporally distributed physical phenomena. The laser heating term  $H$  only applies to the elements in the top layer.  $H$  is integrated on the top surface of the element by assuming that the laser beam has an ideal Gaussian intensity profile and a Beer-Lambert type model is used where laser intensity decreases exponentially with respect to the penetration depth. The convective term  $Q_{conv}$  is used to represent the energy dissipation from a free surface to the ambient environment through heat convection. The conductive term  $Q_{cond}$  includes (1) conduction to neighboring elements along the scanning direction, (2) conduction to build the platform, and (3) conduction to contacting elements in adjacent paths, and (4) conduction to the neighboring layers and powders. The heat conduction is driven by the temperature gradient which is approximated by the finite difference method. The temperature of the element is assumed to be uniform within each element since it is assumed that the Biot number of the element is small, in other words, the element is assumed to be small enough so that it is determined to be "thermally simple". Readers can refer to paper [3] for more details.

### 3. Modifications and improvements on Contact-Aware Path-Level (CAPL) thermal simulation

CAPL originally focused on the FDM process and made corresponding assumptions. Modification is needed to use CAPL to simulate the laser scanning on the solid surface. In this section, we first identify the modifications that are needed for CAPL to be consistent with implementation details in the NIST AMMT dataset. We then discuss the necessary modifications and improvements to address these discrepancies. (see Figure 1).

To attempt to improve the simulation results and better utilize and align with available data, We identified three needed modifications to be consistent with implementation details in the NIST AMMT dataset. Firstly, the original CAPL requires all the elements must be associated with a segment of scanning paths. The elements represent the powder materials that will be scanned and solidified. The widths of these elements will be dynamically grown in the execution stage to mimic the powder melting process. However, the AMMT data used is obtained on a solid surface. Because it is a continuum all the volume needs to be discretized and accounted for in the simulation no matter if scanning paths go through it or not. Also, since there is no powder melting process on the solid surface, the element growth is not applicable on the base layer.

Secondly, the original CAPL approach requires the element to have no overlap with other elements. The element

contacts needs to be orthogonal since all elements have a similar rectangular shape. But in the PBF process, it is common to have overlapping paths since it is possible to remelt the solidified powder. In addition, the scan strategy used for the NIST experiment has nonparallel paths (see contour and infill in Figure 2). Unexpected overlap or void will occur when addressing the general non-parallel paths, as shown in Figure 3.

Lastly, the original CAPL uses the forward Euler method (a first-order explicit method) for thermal simulation and assumes a small Biot number ( $Bi = hL/k$ , where  $h, L, k$  is the convection coefficient, characteristic length, and conductivity of the element) for the element. In the FDM process, elements usually can satisfy this assumption due to the scanning speed being relatively slow compared to the PBF process. Here, however, a small element length ( $\sim 10 \mu m$ ) is required to ensure enough resolution to capture the melt pool length, but the element width is too large since the hatch space is too large (100  $\mu m$  here). This means the Biot number in the width direction will be an order larger than that in the length direction and should be reflected as such in a PBF model. In the lumped model, thermal conduction between two elements  $i$  and  $j$  is computed as  $Q_{cond} = kA\Delta T_{ij}/d_{ij}$  where  $k$  is the conductivity,  $A_{contact}$  is the conduction area, and  $d_{ij}$ , and  $\Delta T_{ij}$  are the distance and temperature difference between the two elements. Considering the elements here (see Figure 3), a naive implementation of the lumped model will lead to insufficient heat conduction in the direction where the characteristic length is too long.

#### 3.1. Representing solid surface with fictitious elements

For the first improvement, we modify the path-level discretization algorithm in the pre-processing stage to account for solid continuums. We add additional fictitious paths so that the entire domain is filled with real paths and fictitious paths. The contacts between all elements are initialized according to the contact graph. We initialize all elements with solid material properties since a solid surface is used in the present paper. Since no powder melting is involved in the present paper, we suppress the element growth mechanism. For the present paper, the fictitious paths are the contours around the real scanning paths, as shown in Figure 2.

#### 3.2. Elements initialization by Voronoi diagram

To address the second improvement, we modify the path-level discretization algorithm with a new elements width initialization algorithm by the Voronoi diagram. The element width will be no longer updated in the execution stage since we suppress the element growth mechanism as discussed above. In the new element width initialization algorithm, we initialized all element widths with a small number ( $W_0 = 10\mu m$ ). After initialization, we increase the element widths simultaneously. For each element, we stop the increase of width once the element's overlap with other elements exceeds a given threshold  $s$  ( $3 \times 10^{-11} m^2$  used here). The element width initialization ends when all elements stop growing wider. Such element width initialization procedure approximately generates a



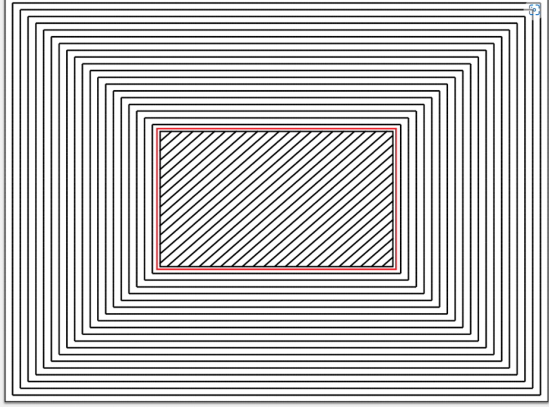


Figure 2: The actual laser path is inside the red box. Fictitious elements are added as the paths outside the red box to represent the larger surface. The solid continuum is modeled as multiple such layers.

Voronoi diagram, whose cells have the path segments as their site, see Figure 3.

We use an in-process laser power normalization for the second needed modification in addition to the element width initialization by the Voronoi diagram. Note there are some overlaps and voids between the elements initialized by the Voronoi diagram. When a laser scans through these elements, the voids and overlaps will cause the total laser power input to artificially fluctuate. The in-process laser power normalization is a modification of the lumped-capacitance heat transfer model to correct for this artificial fluctuation. In the lumped model, every element takes the laser energy input. The total laser energy input on all elements should be equal to  $\alpha P$  (laser power  $P$  multiplies absorptivity  $\alpha$ ) because of energy conservation:

$$\sum_i^N H_i(t) = \alpha P \quad (1)$$

where  $H_i(t)$  is the laser energy input term of the element  $i$ . Theoretically  $N$  should be the number of all elements which are exposed to laser energy input. Here, we use the number of elements inside the active body as  $N$ . This approximation is due to the assumption of thermal localization by utilizing an active body. The total energy could be higher or lower than the input laser term because of the overlap and void. To mitigate this problem, we normalize the input laser power  $P$  during the simulation process by a constant  $\alpha P / \sum_i^N H_i$ . In other words, the laser power at  $t$  should be:

$$P(t) = \frac{\alpha P}{\sum_i^N H_i} P \quad (2)$$

in which  $P$  is the nominal laser power, and  $P(t)$  is the normalized laser power to replace  $P$  in equation 1.

### 3.3. Improved conduction model

The third improvement addresses the lumped thermal model for the elements. Here we correct a previously underestimated temperature gradient, which is originally approximated by the finite difference method. For example,

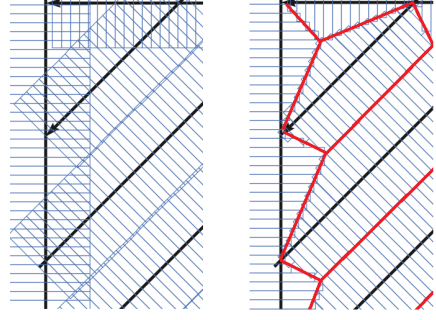


Figure 3: Example of elements on the left top corner of the layer. Unexpected element overlaps with non-parallel overlapped path exists before modification (left). Elements generated by Voronoi diagram after modification (right): elements (in blue) approximately form a Voronoi diagram (in red) whose sites are the scanning paths (in black)

the original conduction energy is given as  $kA_{contact} \frac{\Delta T_{ij}}{d_{ij}}$ , where the conduction characteristic distance is  $d_{ij}$  which is the distance between two elements  $i$  and  $j$ . In a real melt pool, the temperature spatial gradient is very high around the melt pool (temperature spatially decays from the melting point to a much lower temperature in a relatively short distance). When the element width is too large, the same temperature decay will be artificially assumed to happen at a much larger distance (the element width), thus the side-by-side conduction will be underestimated. To address this issue, we cap the conduction characteristic distance by thresholding the conduction characteristic distance. Here we assume the threshold  $d_0$  to be a constant which equals to the maximal element length (here is 10  $\mu\text{m}$ ). Since here element length is much smaller than the element width, the threshold  $d_0$  ensures the thermal conduction  $Q_{cond}$  in both the scanning direction and the transverse direction has the same order of magnitude. The conduction term between two elements  $i$  and  $j$  is to be modified as

$$Q_{cond} = \frac{kA_{contact} \Delta T_{ij}}{\max(d_0, d_{ij})} \quad (3)$$

Due to the existence of overlapped elements, we redefine the contact area as the projection area (the projected angle is  $\theta$ ) of the intersected cross-section (see Figure 4):

$$A_{contact} = \min(A_{cs1}, A_{cs2}) / \sin \theta \quad (4)$$

where  $A_{cs} = W \times H$

## 4. Validation of PBF-CAPL through Melt Pool shapes

### 4.1. Validation Dataset Overview

The experiment dataset used for validation of the modified CAPL consists of melt pool frames acquired on the Additive Manufacturing Metrology Testbed built by

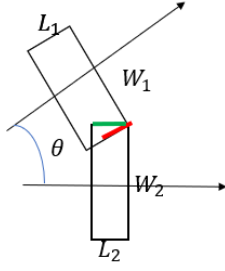


Figure 4: Top view of the contact area (in red). The contact area is the smaller projected cross-section (in green) projected along the angle  $\theta$  between two elements.  $L$  and  $W$  are the element length and width. Arrows indicate the scanning directions.

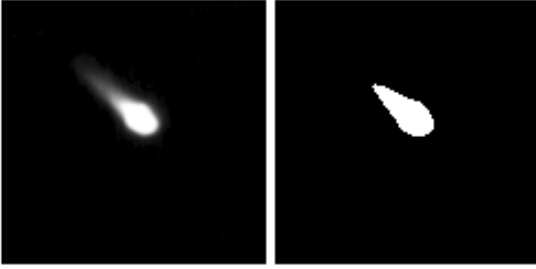


Figure 5: An example of melt pool frame (left) acquired on the Additive Manufacturing Metrology Testbed by NIST and the binarized result (threshold is 80 out of 255).

NIST. The resolution of each frame is approximately 7.13  $\mu\text{m}/\text{pixel}$ . An example of the melt pool frame is shown in Figure 5. A threshold of the digital value corresponding to the melting temperature is needed to extract the melt pool shape. Based on other experiments conducted on AMMT [12], we use 80 out of 255 as the threshold (see Figure 5). The melt pool shape is approximated by the Python library scikit-image's `skimage.measure.regionprops` function (equivalent to MATLAB's `regionprops` function), which approximates the melt pool shape by an ellipse that has the same normalized second central moments as the region. The melt pool length and width are computed as the length of the major and minor axis.

We use the first 10 cases from the dataset with varying laser power and every case consists of 1498 melt pool images at various locations during the laser scan. The scanning paths are shown in Figure 6 and all 10 cases use the same scanning path. There are in total 39 scan vectors which are labeled in Figure 6. The laser scanning speed for all 10 cases is the same and is shown in Figure 7. Note the laser is turned off while overshooting outside the scanning region to ensure constant scanning speed inside the scanning region. For ease of discussion, we classify scan vectors into different groups, including 4 contour vectors and 35 diagonal raster scan vectors inside the contours (see Figure 6). The 10 cases differentiate from each other by the laser power being used (see Figure 8). Case 01 has the highest laser power which is constant (195 W), and all other cases have variable and lower laser power. For example, the laser power of Scan 01 for all cases and the

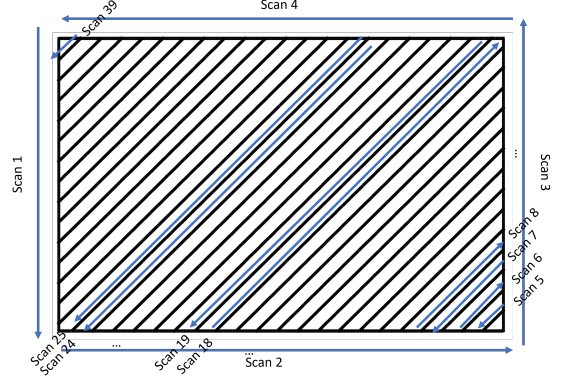


Figure 6: Numbering of scan vectors.

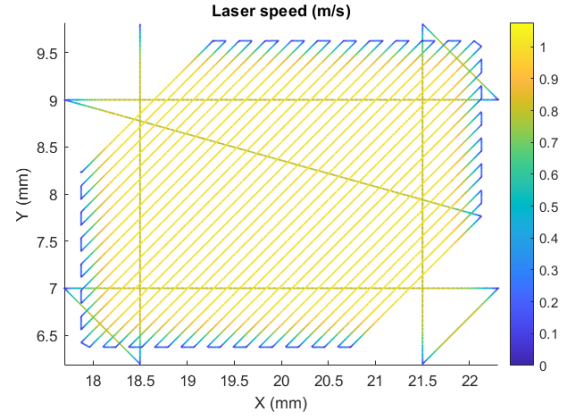


Figure 7: Laser speed map for Case 01. All 10 cases have the same identical speed map only different by their relative locations. Only Case 01 has constant laser power.

laser power of Scan 19 - Scan 24 for Case 03 are shown in Figure 9, in which the laser power is plotted as a function of the distance along the scanning direction. The laser power was lowered to decrease the variance in melt pool size based on the residual heat factor in an earlier NIST study. Interested readers may refer [12] for details. For every case, the 1498 melt pool images come from sampling on a single-layer scanning on an Inconel 625 solid surface. The images come from an even sampling at the frequency 20kHz when the laser is turned on.

All melt pool lengths from the experimental melt pool image data are plotted as line graphs shown in Figure 10. The vertical axis represents the melt pool length, and the horizontal axis represents the frame number. Since the scanning path is geometrically the same for all cases and the frames are sampled at the same time sequence, the same frame number results in the same relative location in every case.

In all cases, we observe that the melt pool lengths periodically drop to zero. This is due to a synchronization issue of the melt pool monitoring system such that the first image at the beginning of each scan is captured before the laser starts. In addition, excessively long melt pools are

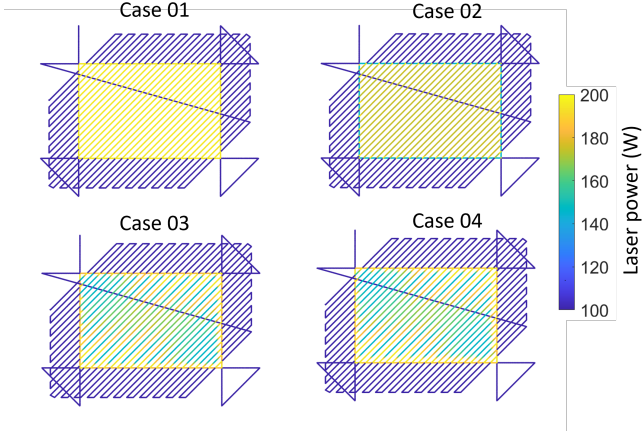


Figure 8: Laser power map for cases 01 - 04. The dark blue here indicates no power. From Case 02, all cases have variant laser power and they differentiate from each other by how the laser power distributes.

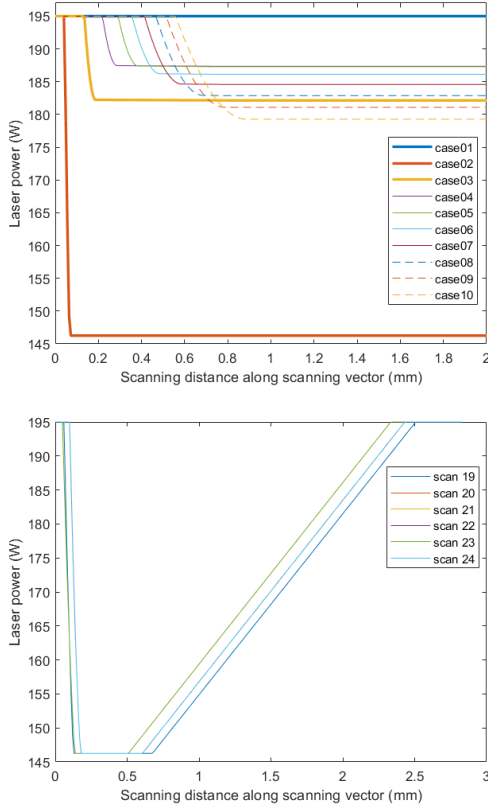


Figure 9: Laser power plotted as a function of distance along the Scan 01 for all cases (top). The distance range from 0 to 2 mm because the length of Scan 01 is 2 mm for all cases. The laser power of scan 19 - 24 for case 03 is shown at the bottom. Scan 19 - 24 have adjacent parallel scan vectors which have the same length.

Table 1: Process parameters and material properties of IN625[52]

Solidus temperature $T_S$ (K)	1563
Liquidus temperature $T_L$ (K)	1623
Environmental temperature (K)	293
Latent heat of fusion (kJ/kg)	290
Specific heat ( $T \leq T_S$ ) (J/kg K)	$339 + 0.24T$
Specific heat ( $T \leq T_L$ ) (J/kg K)	735
Thermal conductivity, ( $T \leq T_S$ ) (W/(m K))	$5.3 + 0.015T$
Thermal conductivity, ( $T \leq T_S$ ) (W/(m K))	30.05
Density kg/m <sup>3</sup>	8440
Convection coefficient (W/(m <sup>2</sup> K))	10
Substrate temperature (K)	293
Laser spot diameter ( $\mu$ m)	85

observed near the beginning of some scan vectors. Upon closer examination, this is due to the gas plume being mischaracterized as the melt pool after thresholding (see Figure 11). In both these cases, the extracted melt pool lengths do not correspond to the real melt pool length, therefore, are considered outliers in the CAPL validation.

#### 4.2. Calibration of process parameters and material properties

Melt pool length from CAPL simulation is directly computed by measuring the maximum distance between two melted elements. We use all material properties but absorptivity from [52] for simulations in the present paper. Material properties including specific heat and conductivity are modeled as functions of temperature (see table 1). Phase changes due to melting or solidification are handled by the equivalent specific heat formulation [52, 53].

The absorptivity is calibrated with Case 01 of the dataset and used for the remaining cases. We calibrated absorptivity because it has a significant influence on thermal history and it can significantly vary when the surface conditions vary. Understanding absorptivity and surface conditions itself can be an important topic where many studies have been conducted [54, 55]. We note that the absorptivity of laser power may depend on a variety of factors and is not a constant in general, but it is a common practice that constant absorptivity is used for simplification. In the present paper, we choose 0.43 as it minimizes the error of melt pool length in Case 01. This value is consistent with the ranges provided by the literature. For example, the absorptivity of In625 solid surface ranges from 0.4 to 0.9 [56]. This value is applied to other cases in the subsequent tests.

Experimental data and simulation results of melt pool lengths, as well as the error percentages, are plotted in Figure 12. We observe a consistent match between the experimental data and simulation results with about 10 percent of relative error in all cases as shown in table 2. The comparison between simulation results and experimental data will be discussed in detail in the rest of this section.

#### 4.3. Melt pool length validation

##### 4.3.1. Melt pool length evolution within scan vector

Firstly we discuss the melt pool length evolution on the same scan vector. We categorized the results into two groups: contour scan vector (we will use Scan 01 as an

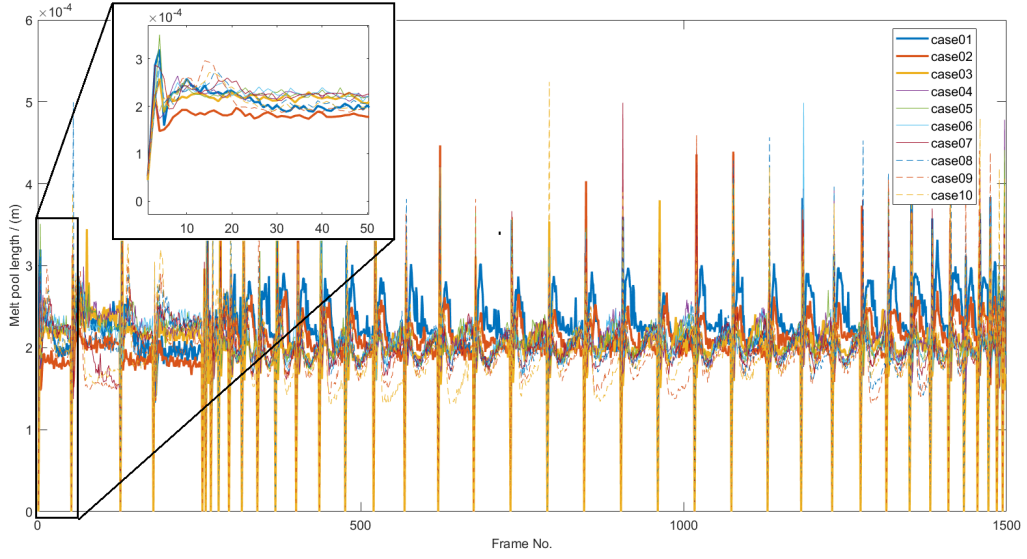


Figure 10: Experimental melt pool length for all 10 cases  $\times$  1498 frames. Zoom in view of Scan 01 is shown. Zero melt pool length is due to the MPM system skipping the first frames of the scan vectors.

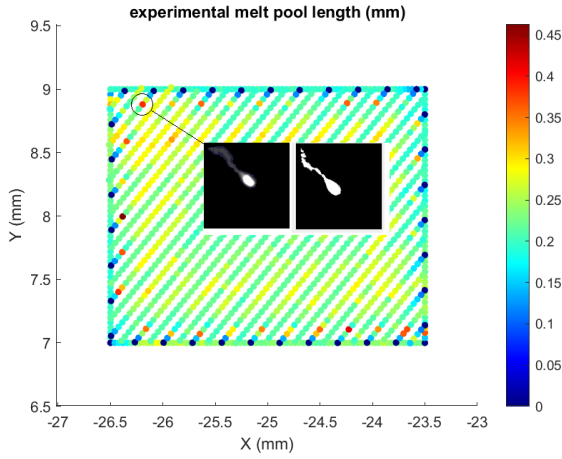


Figure 11: Melt pool image with plume and the binarized results. Plume leads to incorrect melt pool length extracted value. These incorrect values are shown in the length map as red dots.

example) and 45-degree scan vector (we will use Scan 19 - 24 as examples).

We choose Scan 01 since it can be considered a single-scan test without thermal inference from other scan vectors. Because it is the first scan vector and there is no laser scanning on the surface yet before Scan 01 is applied, Scan 01 should be free from the influence of other scan vectors. Therefore the evolving melt pool shape on it should just reflect the influence from Scan 01. We also choose Scan 19 - 24 in Case 01 because (a) they are parallel and identical to each other and all scan vectors have constant laser power, and (b) we observed melt pool length evolves similarly on these scan vectors (see Figure 14).

On Scan 01, we plot melt pool length as a function of scanning distance on the scan vector and show the results

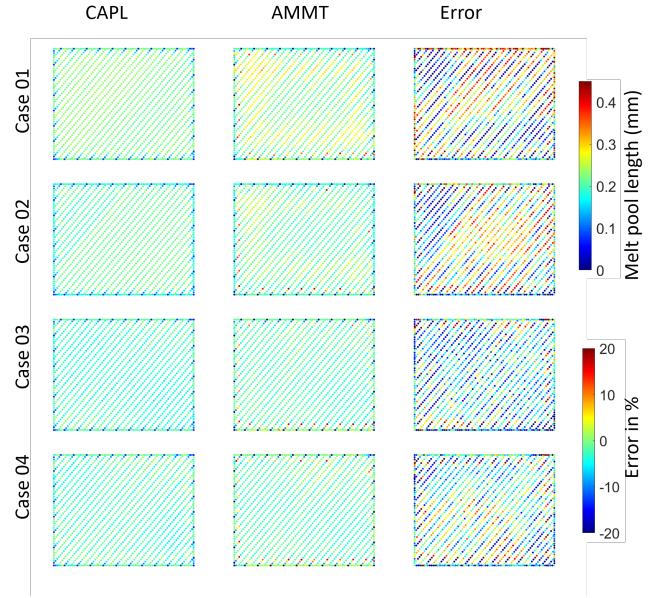


Figure 12: AMMT experimental results of melt pool length map for cases 01, 02, 03, and 04 (middle) and the corresponding CAPL simulation results (left) and the relative errors in percentage (right). AMMT and CAPL results share the same color bar.



of cases 01, 02, and 03 in Figure 13. An increase in melt pool length at the beginning of the laser scan, i.e. “bump”, is observed in Case 01: melt pool length firstly increases and then decreases as the laser moves on the scan vector. We also observed the bump on the 45-degree scan vectors (see Figure 14) of Case 01. The CAPL simulation does not predict such a bump in these cases. One possible reason for this discrepancy is that we use constant absorptivity in modified CAPL simulation. This is because we observe that the magnitude of the bump is related to the laser power. For example, comparing the melt pool length on Scan 01 in different cases, the bump is much less obvious in cases 02 - 07, where relatively lower power is applied shortly after at the beginnings of the scan vectors. The CAPL simulation matches well with experimental data in these cases (see Figure 15 and Figure 16). We will discuss the increase in melt pool length at the beginning of the laser scan in Section 5.

The effects of varying laser power on the length of the melt pool are also predicted by the CAPL simulation. We give examples in Figure 17, where the mean values of melt pool length on Scan 01 and Scan 24 are plotted with respect to the case number. We observed that CAPL captures a similar trend as shown in experimental data: on Scan 01, Case 02 has the smallest average melt pool length, and then the average melt pool length increases from Case 03 and then decreases again from Case 07. On Scan 24, both CAPL and experimental data suggest the smallest average melt pool length is in Case 09 and the largest average value is in Case 01.

#### 4.3.2. Scan-wise melt pool length evolution

In this section, we discuss the melt pool length evolution across the scan vectors. The average melt pool length of each scan vector is shown in Figure 18. From Scan 05 to Scan 39, melt pool lengths first increase, then plateau, and finally drop. This trend is consistent with the lengths of these scan vectors. The length of the scan vector starts as short with Scan 05 at the right bottom, reaches the maximum at Scan 19 and plateau, and decreases again to the last Scan 39. The scan vector averaged melt pool length is short when the total scan vector length is short and vice versa. This is because the melt pool needs the scan vector to be long enough to have its tail formed. On each scan vector, the melt pool always starts with a relatively round shape and gradually evolves into a tear shape as the laser moves (see Figure 19). A scan vector that is too short will be dominated by the melt pool shape without tails.

The scan vector length is not the only factor that affects the melt pool length. In both the experiment data and modified CAPL simulation results, we observed some trends which could be explained by the influence of reheating from adjacent scan vectors. As shown in Scan 19-24 in Case 01, the difference in melt pool length between the neighbor scan vectors seems negligible. It seems the reheating from the adjacent scan vectors is negligible since Scan 24 has a comparable melt pool length to that in Scan 19. However, it is interesting to note that, even though they have identical scan vector lengths, Scan 39 always has a longer melt pool length compared to Scan 05. Note that Scan 05 is the first 45-degree scan vector and Scan 39 is likely due to the accumulation of residual heat in the

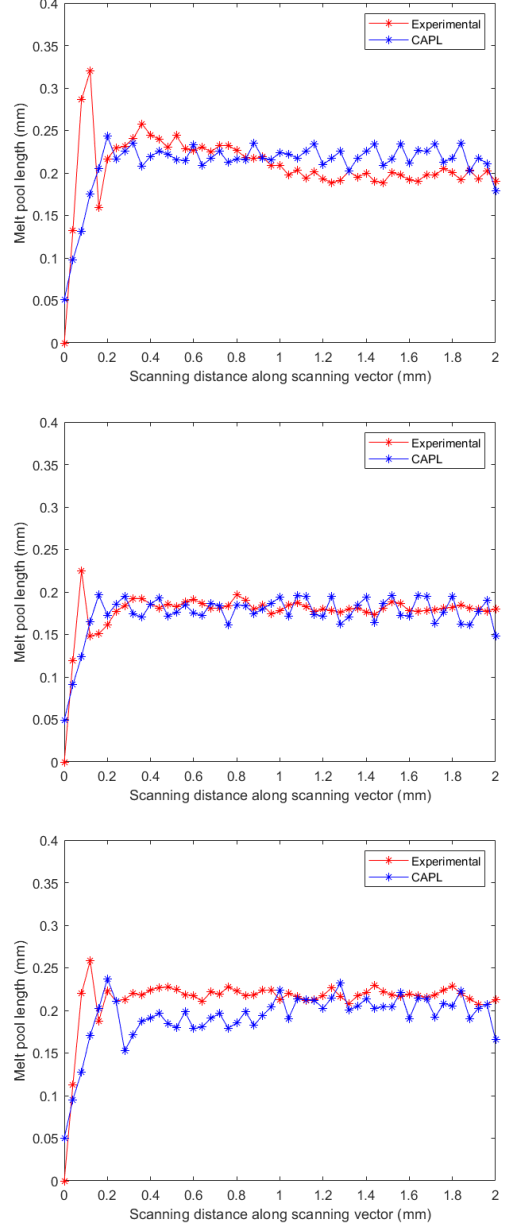


Figure 13: Melt pool length for Scan 01 of Case 01, Case 02, and Case 03. A bump at the beginning of the scan vector in experimental data is not predicted by CAPL in Case 01. Laser power along the scan vector can be found in Figure 9.

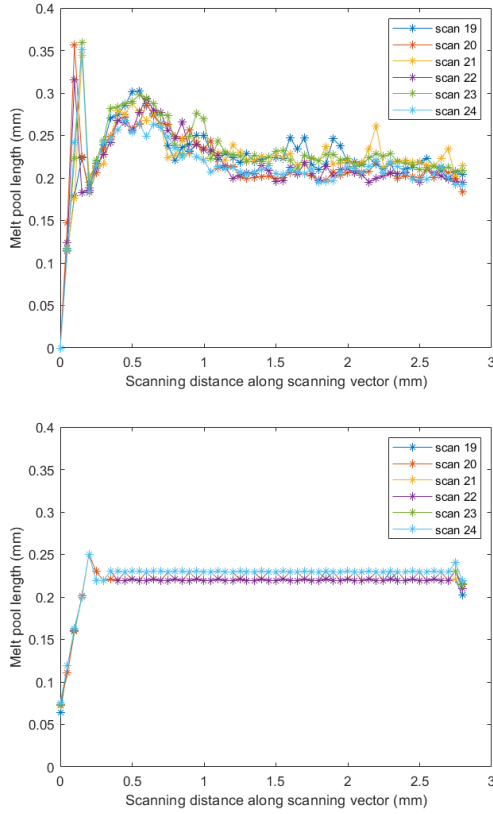


Figure 14: Experimental (top) and simulation (bottom) melt pool length of Scan 19-24 for Case 01. Laser power is constant (195 W). The CAPL approach does not predict the bump.

Table 2: Relative error of melt pool length predicted by CAPL

Case No.	01	02	03	04	05
Relative error (%)	11.11	9.80	9.62	8.81	8.44
Case No.	06	07	08	09	10
Relative error (%)	8.21	8.87	9.03	11.66	12.70

scanning progress. Similar situations can be also found in other cases, see Figure 18. This also might be due to the reheating from the adjacent scan vectors, and this effect is only significant at the beginning of the scan vector where the melt pool is relatively round without a tail.

#### 4.4. Melt pool width validation

The CAPL simulation results cannot be directly used to obtain the melt pool width because they are only defined on the scanning paths. In the present paper, we obtained the melt pool width from the reconstructed melt pool based on the CAPL simulation results. We reconstruct the melt pools by using inverse distance weighted interpolation of temperature distribution. Since the temperature for every element at any specific time is available, the temperature at any location can be given by interpolation:

$$T(x) = \frac{\sum_i^N w_i(x) T_i}{\sum_i^N w_i(x)} \quad (5)$$

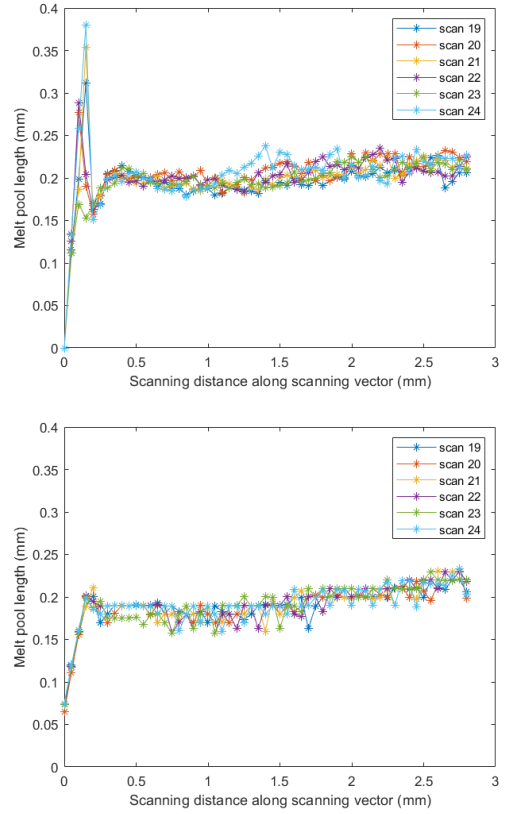


Figure 15: Experimental (top) and simulation results (bottom) of Scan 19 - 24 in Case 03. The bump disappeared in experimental data, and the trend in experimental data is captured by simulation results. The laser power of these scans can be referred to in Figure 9.

where  $w_i(x) = \frac{1}{d(x, x_i)^p}$  is the power  $p$  of the inverse of distance between element  $i$  and location  $x$  (We use  $p = 1.3$  here which minimizes the errors).  $N$  is the number of elements inside the active body. In the present paper, we interpolate the melt pool shape on a  $0.96 \text{ mm} \times 0.96 \text{ mm}$  region with a  $120\text{-pixel} \times 120\text{-pixel}$  frame. An example of such interpolation is given in Figure 20. We obtain the melt pool width by the same approach used for experimental melt pool width with the interpolated temperature distribution: melt pool width is the length of the minor axis computed by the regionprops function with the given interpolated temperature distribution.

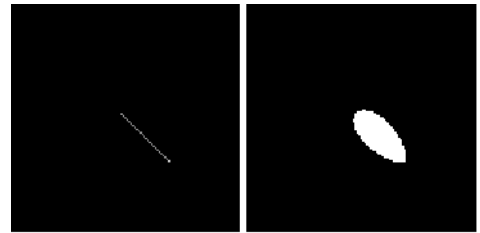


Figure 20: Melt pool from CAPL (left) and its interpolation (right).

Melt pool width from the experiment dataset and pre-

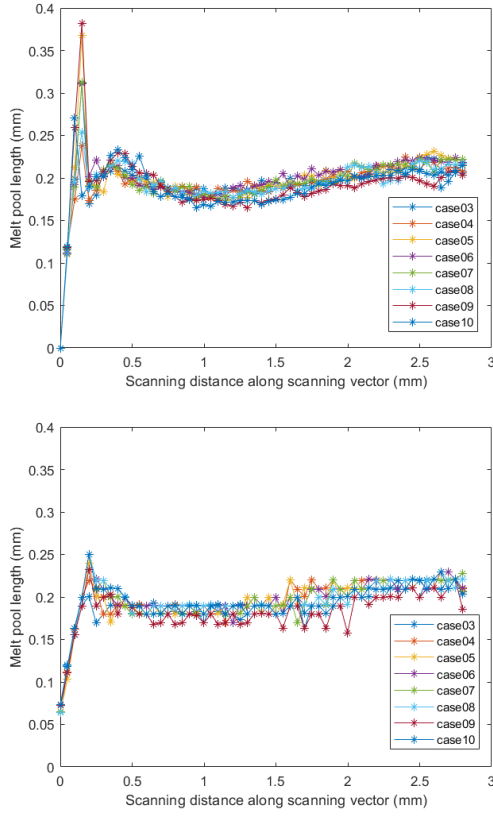


Figure 16: Scan 19 in Case 03 - Case 10 as a function with respect to scan distance. AMMT data (left) vs CAPL simulation results (right).

Table 3: Relative error of melt pool width predicted by interpolation of CAPL results

Case No.	01	02	03	04	05
Relative error (%)	9.80	6.93	8.62	8.753	9.50
Case No.	06	07	08	09	10
Relative error (%)	9.90	10.64	9.99	13.71	9.36

diction by CAPL through interpolation and the relative errors are shown in figure 21. The averaged relative errors for all cases are reported in table 3. The melt pool width has less variation compared with the melt pool length. For example, the melt pool width evolution of the Scan 19 is plotted as a function of scanning distance along the scan vector in Figure 22). Note that laser power is not constant in Cases 02, 03, and 05, but both CAPL simulation results and experimental data suggest melt pool width has very little variation compared with the melt pool length in a scan vector like it is in Case 01 (see Figure 14), indicating that the melt pool width is less sensitive to laser power than the melt pool length.

## 5. Conclusion and future directions

We developed an improved path-scale PBF thermal simulation approach based on contact-aware path-level (CAPL) discretization. We validate the proposed approach with melt pool shapes acquired by the Additive

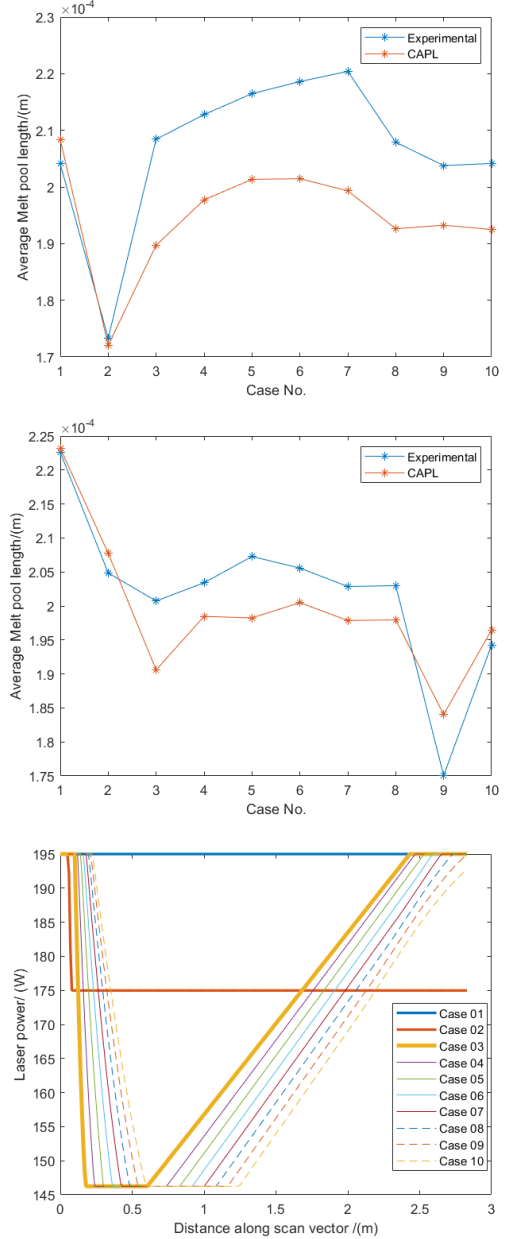


Figure 17: Mean value of melt pool length on Scan 01 (top) and Scan 24 of Case 01 to Case 10 (middle) and laser power on Scan 24 (bottom). CAPL predicts a similar result compared with experimental data.

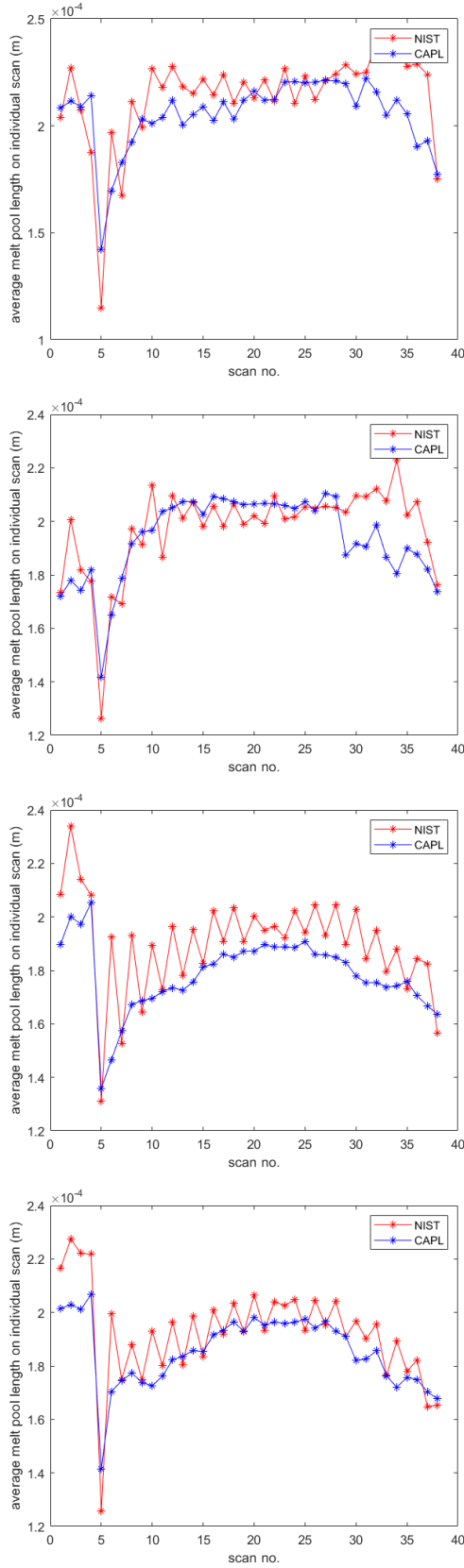


Figure 18: Scan-wise average melt pool length, Case 01, 02, 03, 05. The oscillation of experimental data is due to the perturbation of plume frames.

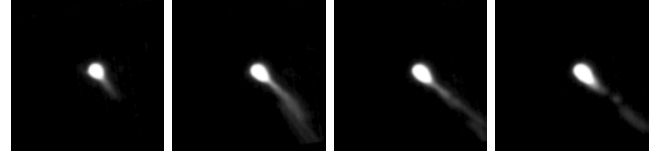


Figure 19: Experimental frames of Scan 39 in Case 01. Scan 39 is the last scan vector and only has four melt pool frames. The melt pool evolves from a relatively round shape to a tear shape.

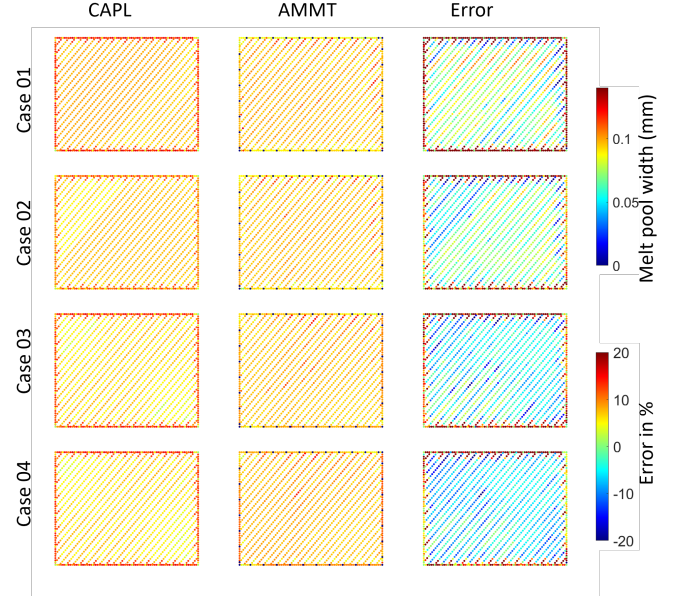


Figure 21: Experimental (AMMT) melt pool width map (middle), the interpolation results based on CAPL simulation results (left), and the relative errors in percentage (right) for cases 01 - 04. AMMT and CAPL results share the same color bar.

Manufacturing Metrology Testbed (AMMT) built by the National Institute of Standards and Technology (NIST). We demonstrated that the proposed approach achieves a good match of the melt pool length and width compared with the experimental data. We also discussed the influence of laser power on the thermal history at the path-scale level.

One source of error during the CAPL validation is the increase in the difference in melt pool length at the beginning of the laser scan while the laser power and speed remain constant in Case 01. This is likely due to the use of constant absorptivity in the current work, which is widely assumed among LPBF thermal history simulations [43, 57, 58]. Such an assumption results in an underestimation of the absorptivity at the beginning of high-power scan vectors during the calibration, for example in Case 01 and Case 09 (see Figure 24). Experimental measurements have observed absorptivity to change throughout the laser scan path [54, 56, 59]: (a) an initial rise due to the shiny plate melting increasing surface roughness, (b) a subsequent drop due to the liquid melt pool formation and increased reflectivity, (c) the second rise due to the formation of the keyhole, and (d) eventually a keyhole-related



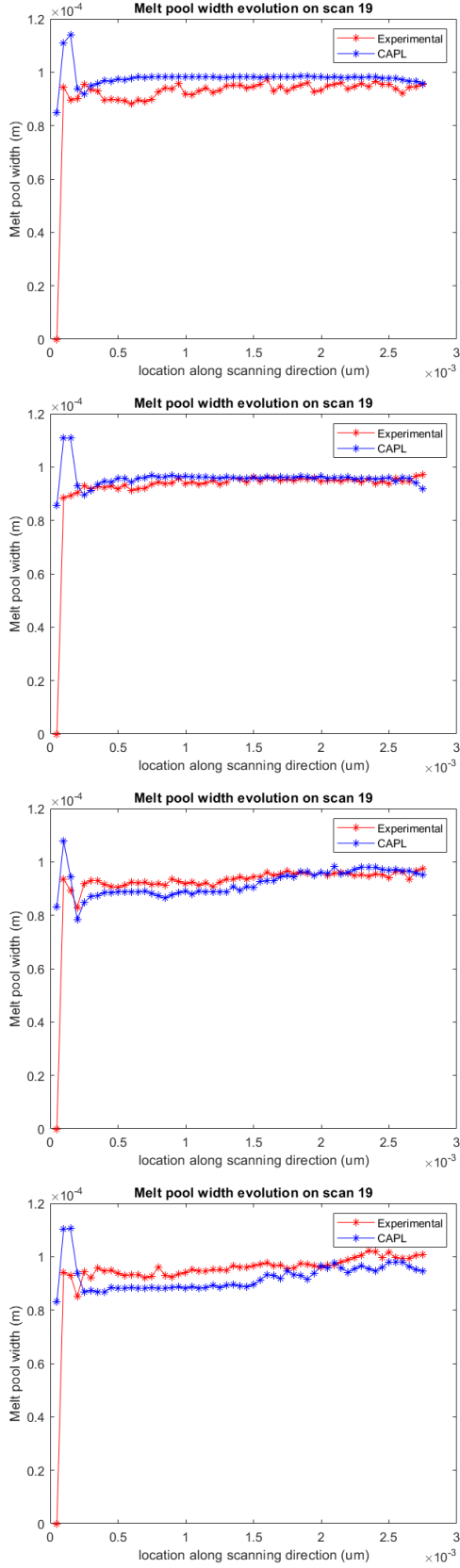


Figure 22: Melt pool width on Scan 19 of Cases 01, 02, 03, and 05. Both experimental data and CAPL simulation results show a relatively constant evolution.

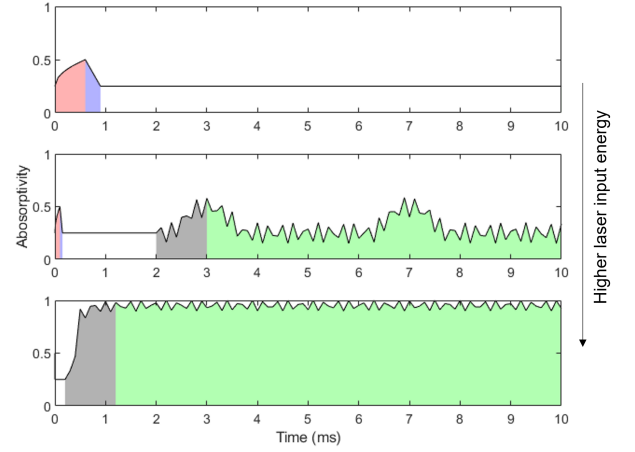


Figure 23: A schematic of dynamic laser absorptivity reproduced from paper [59]. The top, middle, and bottom are the dynamic absorptivity under the conduction model, transition model, and key-hole model. The different models are determined by the laser input energy density. Stages (a, in red) and (b, in blue) are mostly visible in the conduction model, while in keyhole model is dominated by stages (c, in black) and (d, in green). In the transition model, all four stages are visible and there is low-frequency keyhole oscillation.

high-frequency periodic oscillation. A dynamic laser absorptivity depending on the time and distance of the laser start as well as the condition inside the melt pool therefore will better capture the melt pool behavior near the beginning of the laser scan.

Based on this observation, we create a simplified model that captures the laser absorptivity trend in stages (a) and (b). We assign the absorptivity by a piecewise linear model (see Figure 26) in the range from 0 to 0.8 mm. A constant absorptivity (0.41) is assigned to the rest of the scan vector. We apply this simplified model to Case 01. The results are shown in Figure 25. The dynamic laser absorptivity model not only results in a better overall prediction of the melt pool length but also reproduces the “bump” seen at the beginning of the scan (see Figure 26). A more accurate laser absorptivity that is based on physical testings and models the keyhole behaviors in stages (c) and (d) is outside the scope of the current discussion and will be studied as part of future work to further improve the CAPL approach.

The second future improvement is to better predict the melt pool width as well as the shape of the melt pool. Recent progress in machine learning has enabled an exponential increase in research into leveraging machine learning to predict and control additive manufacturing processes [60, 61, 62]. We are exploring a conditional Generative Adversarial Network (cGAN) -based approach [63, 64, 65] to predict the melt pool image based on the thermal history along the laser scan path. GAN uses its generator to generate candidates and uses its discriminator to evaluate the candidates. The generator and the discriminator are trained so that eventually the generator is able to predict accurate melt pool frames. The data pair of thermal history and melt pool images for neural network training and validation are obtained through CAPL and

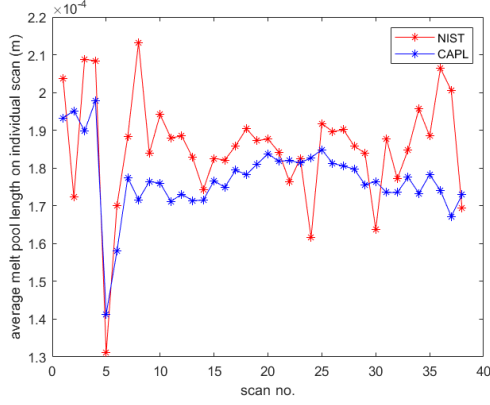


Figure 24: Scan-wise average melt pool length, Case 09. Relatively large errors are observed at around Scan 05 and Scan 39, where high laser power is used.

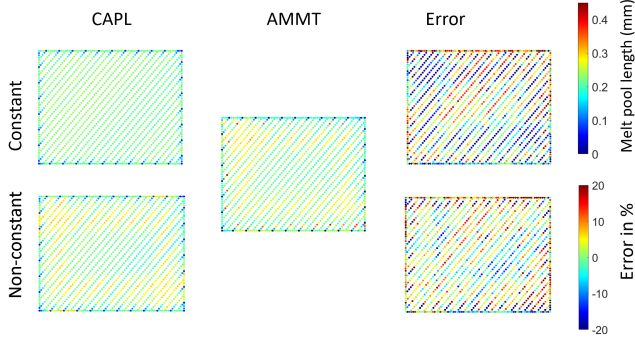


Figure 25: CAPL results of Case 01 with the non-constant absorptivity surrogate model (higher absorptivity at beginning of every scan) on the bottom and the results with constant absorptivity on top. Mean error is smaller (9.10%) compared with no surrogate model (11.11%) shown in table 2. The underestimation of the "bump" can be seen improved with the non-constant model.

AMMT data, respectively (see Figure 28). Specifically, we snapshot the thermal history into a series of thermal distribution images that matches the field-of-view and time steps of the captured melt pool images to work as the conditional inputs into the cGAN. Compared to the interpolation approach discussed in Section 4, the machine learning-based approach better captures the overall shape of the melt pool, which, in turn, provides further insight into the steep thermal gradient inside the melt pool. We will validate the prediction of the melt pool images through geometric characteristics, including length, width, and angle, of the melt pool as part of future work. Such a machine learning model could be used to improve the modified conduction model in the present paper. For example, here the conduction characteristic distance  $d_0$  is a constant, and its machine learning model could be used to map this quantity as a function of process parameters to further improve accuracy.

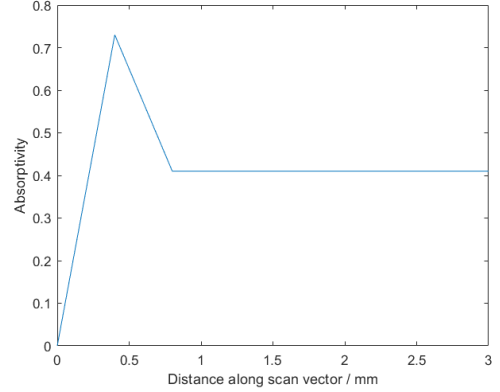
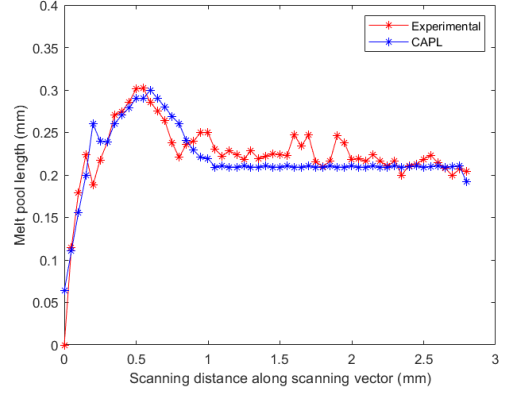
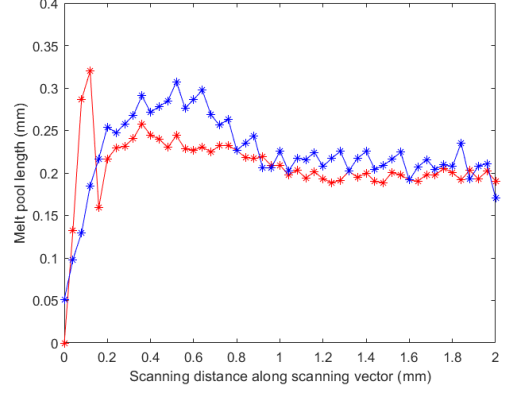


Figure 26: CAPL results of Case 01 with the surrogate model of Scan 01 (top) and Scan 19 (middle). The "bump" can be reproduced by the piecewise linear surrogate absorptivity model (bottom). The peak value of the surrogate model is 0.73.

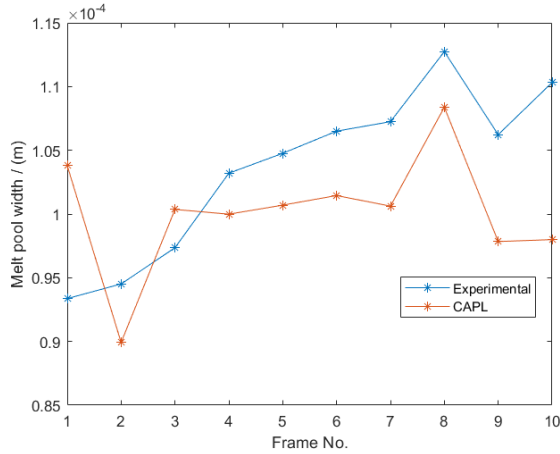


Figure 27: Average of melt pool width of Scan 01, Case 01-Case 10.



Figure 28: An example of melt pool prediction by machine learning. The left, middle, and right are the input, ground truth, and prediction respectively.

## Acknowledgements

The authors thank Ho Yeung from the National Institute of Standards and Technology for providing the melt pool monitoring data and helpful discussions. This research was supported by the National Institute of Standards and Technology. The responsibility for errors and omissions lies solely with the author.

## References

- [1] Y. Zhang, V. Shapiro, Linear-time thermal simulation of as-manufactured fused deposition modeling components, *Journal of Manufacturing Science and Engineering* 140 (7).
- [2] Y. Zhang, V. Shapiro, P. Witherell, Towards thermal simulation of powder bed fusion on path level, in: *International Design Engineering Technical Conferences and Computers and Information in Engineering Conference*, Vol. 59179, American Society of Mechanical Engineers, 2019, p. V001T02A034.
- [3] Y. Zhang, V. Shapiro, P. Witherell, A scalable framework for process-aware thermal simulation of additive manufacturing processes, *Journal of Computing and Information Science in Engineering* 22 (1).
- [4] S. Vock, B. Klöden, A. Kirchner, T. Weißgärber, B. Kieback, Powders for powder bed fusion: a review, *Progress in Additive Manufacturing* 4 (4) (2019) 383–397.
- [5] V. Bhavar, P. Kattire, V. Patil, S. Khot, K. Gujar, R. Singh, A review on powder bed fusion technology of metal additive manufacturing, *Additive manufacturing handbook* (2017) 251–253.
- [6] D. D. Singh, T. Mahender, A. R. Reddy, Powder bed fusion process: A brief review, *Materials Today: Proceedings* 46 (2021) 350–355.
- [7] R. Acharya, J. A. Sharon, A. Staroselsky, Prediction of microstructure in laser powder bed fusion process, *Acta Materialia* 124 (2017) 360–371.
- [8] A. Hilaire, E. Andrieu, X. Wu, High-temperature mechanical properties of alloy 718 produced by laser powder bed fusion with different processing parameters, *Additive Manufacturing* 26 (2019) 147–160.
- [9] K. Inaekyan, A. Kreitchberg, S. Turenne, V. Brailovski, Microstructure and mechanical properties of laser powder bed-fused in625 alloy, *Materials Science and Engineering: A* 768 (2019) 138481.
- [10] Z. Luo, Y. Zhao, A survey of finite element analysis of temperature and thermal stress fields in powder bed fusion additive manufacturing, *Additive Manufacturing* 21 (2018) 318–332.
- [11] B. Lane, S. Mekhontsev, S. Grantham, M. Vlasea, J. Whiting, H. Yeung, J. Fox, C. Zarobila, J. Neira, M. McGlauffin, et al., Design, developments, and results from the nist additive manufacturing metrology testbed (ammt), in: *2016 International Solid Freeform Fabrication Symposium*, University of Texas at Austin, 2016.
- [12] H. Yeung, B. Lane, A residual heat compensation based scan strategy for powder bed fusion additive manufacturing, *Manufacturing letters* 25 (2020) 56–59.
- [13] E. R. Denlinger, M. Gouge, J. Irwin, P. Michaleris, Thermomechanical model development and in situ experimental validation of the laser powder-bed fusion process, *Additive Manufacturing* 16 (2017) 73–80.
- [14] N. Schnell, M. Schoeler, G. Witt, S. Kleszczynski, Experimental and numerical thermal analysis of the laser powder bed fusion process using in situ temperature measurements of geometric primitives, *Materials & Design* 209 (2021) 109946.
- [15] L. R. Goossens, B. Van Hooreweder, A virtual sensing approach for monitoring melt-pool dimensions using high speed coaxial imaging during laser powder bed fusion of metals, *Additive Manufacturing* 40 (2021) 101923.
- [16] J. A. Mitchell, T. A. Ivanoff, D. Dagel, J. D. Madison, B. Jared, Linking pyrometry to porosity in additively manufactured metals, *Additive Manufacturing* 31 (2020) 100946.
- [17] Y. Lu, Z. Yang, J. Kim, H. Cho, H. Yeung, Camera-based coaxial melt pool monitoring data registration for laser powder bed fusion additive manufacturing, in: *ASME International Mechanical Engineering Congress and Exposition*, Vol. 84492, American Society of Mechanical Engineers, 2020, p. V02BT02A045.
- [18] M. L. G. Grasso, A. Remani, A. Dickins, B. M. Colosimo, R. K. Leach, In-situ measurement and monitoring methods for metal powder bed fusion—an updated review, *Measurement Science and Technology*.
- [19] P. Saunders, D. R. White, Interpolation errors for radiation thermometry, *Metrologia* 41 (1) (2003) 41.
- [20] F. Liebmann, T. Kolat, Exploration of alternative methods for fitting radiation thermometer signal to blackbody temperature, *Fluke Calibration*, American Fork, Utah, USA. Accessed: Jan 10.
- [21] H. Yan, M. Grasso, K. Paynabar, B. M. Colosimo, Real-time detection of clustered events in video-imaging data with applications to additive manufacturing, *IIE Transactions* 54 (5) (2022) 464–480.
- [22] B. M. Colosimo, M. Grasso, Spatially weighted pca for monitoring video image data with application to additive manufacturing, *Journal of Quality Technology* 50 (4) (2018) 391–417.
- [23] J. C. Fox, B. M. Lane, H. Yeung, Measurement of process dynamics through coaxially aligned high speed near-infrared imaging in laser powder bed fusion additive manufacturing, in: *Thermosense: thermal infrared applications XXXIX*, Vol. 10214, SPIE, 2017, pp. 34–50.
- [24] Y. Zhang, G. S. Hong, D. Ye, K. Zhu, J. Y. Fuh, Extraction and evaluation of melt pool, plume and spatter information for powder-bed fusion am process monitoring, *Materials & Design* 156 (2018) 458–469.
- [25] D. Ye, J. Y. H. Fuh, Y. Zhang, G. S. Hong, K. Zhu, In situ

- monitoring of selective laser melting using plume and spatter signatures by deep belief networks, *ISA transactions* 81 (2018) 96–104.
- [26] T. Moran, D. Warner, N. Phan, Scan-by-scan part-scale thermal modelling for defect prediction in metal additive manufacturing, *Additive Manufacturing* 37 (2021) 101667.
  - [27] B. Lane, H. Yeung, Process monitoring dataset from the additive manufacturing metrology testbed (ammt): “three-dimensional scan strategies”, *Journal of Research of the National Institute of Standards and Technology* 124 (2019) 1.
  - [28] B. A. Fisher, B. Lane, H. Yeung, J. Beuth, Toward determining melt pool quality metrics via coaxial monitoring in laser powder bed fusion, *Manufacturing letters* 15 (2018) 119–121.
  - [29] B. Lane, H. Yeung, Process monitoring dataset from the additive manufacturing metrology testbed (ammt): Overhang part x4, *Journal of Research of the National Institute of Standards and Technology* 125 (2020) 1–18.
  - [30] Y. Zhang, V. Shapiro, P. Witherell, A neighborhood-based neural network for melt pool prediction and control, in: *International Design Engineering Technical Conferences and Computers and Information in Engineering Conference*, Vol. 83983, American Society of Mechanical Engineers, 2020, p. V009T09A026.
  - [31] H. Yeung, B. M. Lane, M. Donmez, J. C. Fox, J. Neira, Implementation of advanced laser control strategies for powder bed fusion systems, *Procedia Manufacturing* 26 (2018) 871–879.
  - [32] H. Yeung, B. Lane, J. Fox, Part geometry and conduction-based laser power control for powder bed fusion additive manufacturing, *Additive manufacturing* 30 (2019) 100844.
  - [33] J. G. Michopoulos, A. P. Iliopoulos, J. C. Steuben, A. J. Birnbaum, S. G. Lambrakos, On the multiphysics modeling challenges for metal additive manufacturing processes, *Additive Manufacturing* 22 (2018) 784–799.
  - [34] W. Yan, J. Smith, W. Ge, F. Lin, W. K. Liu, Multiscale modeling of electron beam and substrate interaction: a new heat source model, *Computational Mechanics* 56 (2) (2015) 265–276.
  - [35] A. J. Dunbar, E. R. Denlinger, M. F. Gouge, P. Michaleris, Experimental validation of finite element modeling for laser powder bed fusion deformation, *Additive Manufacturing* 12 (2016) 108–120.
  - [36] Y. Cao, X. Lin, N. Kang, L. Ma, L. Wei, M. Zheng, J. Yu, D. Peng, W. Huang, A novel high-efficient finite element analysis method of powder bed fusion additive manufacturing, *Additive Manufacturing* 46 (2021) 102187.
  - [37] C. Bruna-Rosso, A. G. Demir, B. Previtali, Selective laser melting finite element modeling: Validation with high-speed imaging and lack of fusion defects prediction, *Materials & Design* 156 (2018) 143–153.
  - [38] M. Bayat, A. Thanki, S. Mohanty, A. Witvrouw, S. Yang, J. Thorborg, N. S. Tiedje, J. H. Hattel, Keyhole-induced porosities in laser-based powder bed fusion (l-pbf) of ti6al4v: High-fidelity modelling and experimental validation, *Additive Manufacturing* 30 (2019) 100835.
  - [39] J. L. Bartlett, X. Li, An overview of residual stresses in metal powder bed fusion, *Additive Manufacturing* 27 (2019) 131–149.
  - [40] M. Gouge, E. Denlinger, J. Irwin, C. Li, P. Michaleris, Experimental validation of thermo-mechanical part-scale modeling for laser powder bed fusion processes, *Additive Manufacturing* 29 (2019) 100771.
  - [41] X. Liang, L. Cheng, Q. Chen, Q. Yang, A. C. To, A modified method for estimating inherent strains from detailed process simulation for fast residual distortion prediction of single-walled structures fabricated by directed energy deposition, *Additive Manufacturing* 23 (2018) 471–486.
  - [42] M. Bayat, C. G. Klingaa, S. Mohanty, D. De Baere, J. Thorborg, N. S. Tiedje, J. H. Hattel, Part-scale thermo-mechanical modelling of distortions in laser powder bed fusion—analysis of the sequential flash heating method with experimental validation, *Additive Manufacturing* 36 (2020) 101508.
  - [43] W. Zhang, M. Tong, N. M. Harrison, Resolution, energy and time dependency on layer scaling in finite element modelling of laser beam powder bed fusion additive manufacturing, *Additive Manufacturing* 28 (2019) 610–620.
  - [44] X. Liu, V. Shapiro, Homogenization of material properties in additively manufactured structures, *Computer-Aided Design* 78 (2016) 71–82.
  - [45] M. R. Yavari, K. D. Cole, P. Rao, Thermal modeling in metal additive manufacturing using graph theory, *Journal of Manufacturing Science and Engineering* 141 (7).
  - [46] R. K. Ganeriwala, N. E. Hodge, J. M. Solberg, Towards improved speed and accuracy of laser powder bed fusion simulations via multiscale spatial representations, *Computational Materials Science* 187 (2021) 110112.
  - [47] J. Liu, G. Li, Q. Sun, H. Li, J. Sun, X. Wang, Understanding the effect of scanning strategies on the microstructure and crystallographic texture of ti-6al-4v alloy manufactured by laser powder bed fusion, *Journal of Materials Processing Technology* 299 (2022) 117366.
  - [48] N. Nadammal, T. Mishurova, T. Fritsch, I. Serrano-Munoz, A. Kromm, C. Haberland, P. D. Portella, G. Bruno, Critical role of scan strategies on the development of microstructure, texture, and residual stresses during laser powder bed fusion additive manufacturing, *Additive Manufacturing* 38 (2021) 101792.
  - [49] C. Chen, Z. Xiao, Y. Wang, X. Yang, H. Zhu, Prediction study on in-situ reduction of thermal stress using combined laser beams in laser powder bed fusion, *Additive Manufacturing* 47 (2021) 102221.
  - [50] A. Olleak, Z. Xi, Part-scale finite element modeling of the selective laser melting process with layer-wise adaptive remeshing for thermal history and porosity prediction, *Journal of Manufacturing Science and Engineering* 142 (12).
  - [51] R. Wang, V. Shapiro, Topological semantics for lumped parameter systems modeling, *Advanced Engineering Informatics* 42 (2019) 100958.
  - [52] Y. M. Arisoy, L. E. Ciales, T. Özel, Modeling and simulation of thermal field and solidification in laser powder bed fusion of nickel alloy in625, *Optics & Laser Technology* 109 (2019) 278–292.
  - [53] Y. Zhang, A Scalable Framework for Contact-Aware Thermal Simulation of Additive Manufacturing Processes, *The University of Wisconsin-Madison*, 2020.
  - [54] J. Trapp, A. M. Rubenchik, G. Guss, M. J. Matthews, In situ absorptivity measurements of metallic powders during laser powder-bed fusion additive manufacturing, *Applied Materials Today* 9 (2017) 341–349.
  - [55] M. Matthews, J. Trapp, G. Guss, A. Rubenchik, Direct measurements of laser absorptivity during metal melt pool formation associated with powder bed fusion additive manufacturing processes, *Journal of Laser Applications* 30 (3) (2018) 032302.
  - [56] B. Lane, I. Zhirnov, S. Mekhontsev, S. Grantham, R. Ricker, S. Rauniyar, K. Chou, Transient laser energy absorption, coaxial melt pool monitoring, and relationship to melt pool morphology, *Additive Manufacturing* 36 (2020) 101504.
  - [57] Y. A. Mayi, M. Dal, P. Peyre, M. Bellet, C. Metton, C. Moriconi, R. Fabbro, Transient dynamics and stability of keyhole at threshold in laser powder bed fusion regime investigated by finite element modeling, *Journal of Laser Applications* 33 (1) (2021) 012024.
  - [58] H. Huang, Y. Wang, J. Chen, Z. Feng, An efficient numerical model for predicting residual stress and strain in parts manufactured by laser powder bed fusion, *Journal of Physics: Materials* 4 (4) (2021) 044006.
  - [59] B. J. Simonds, J. Sowards, J. Hadler, E. Pfeif, B. Wilthan, J. Tanner, C. Harris, P. Williams, J. Lehman, Time-resolved absorptance and melt pool dynamics during intense laser irradiation of a metal, *Physical review applied* 10 (4) (2018) 044061.
  - [60] C. Wang, X. Tan, S. Tor, C. Lim, Machine learning in additive manufacturing: State-of-the-art and perspectives, *Additive Manufacturing* 36 (2020) 101538.
  - [61] S. S. Razvi, S. Feng, A. Narayanan, Y.-T. T. Lee, P. Witherell, A review of machine learning applications in additive manufacturing, in: *International Design Engineering Technical Confer-*



- ences and Computers and Information in Engineering Conference, Vol. 59179, American Society of Mechanical Engineers, 2019, p. V001T02A040.
- [62] L. Regenwetter, A. H. Nobari, F. Ahmed, Deep generative models in engineering design: A review, *Journal of Mechanical Design* 144 (7) (2022) 071704.
  - [63] I. Goodfellow, J. Pouget-Abadie, M. Mirza, B. Xu, D. Warde-Farley, S. Ozair, A. Courville, Y. Bengio, Generative adversarial networks, *Communications of the ACM* 63 (11) (2020) 139–144.
  - [64] P. Isola, J.-Y. Zhu, T. Zhou, A. A. Efros, Image-to-image translation with conditional adversarial networks, in: *Proceedings of the IEEE conference on computer vision and pattern recognition*, 2017, pp. 1125–1134.
  - [65] H. Chen, X. Liu, Geometry enhanced generative adversarial networks for random heterogeneous material representation, in: *International Design Engineering Technical Conferences and Computers and Information in Engineering Conference*, Vol. 85383, American Society of Mechanical Engineers, 2021, p. V03AT03A020.